Point Pattern Estimators for Multi-Beam Lidar Scans

Michael T. Benson, Jonathan Nikolaidis, and Garrett M. Clayton

Abstract—In this work, point pattern estimators are used to analyze the distribution of measurements from a multi-beam Lidar on a pitching platform. Multi-beam Lidars have high resolution in the horizontal plane, but poor vertical resolution. Placing the Lidar on a pitching base improves this resolution, but causes the distribution of measurements to be highly irregular. In this work, these measurement distributions are treated as point patterns and three estimators are used to quantify how measurements are spaced, which has implications in robotic detection of objects using Lidar sensors. These estimators are used to demonstrate how a pitching trajectory for the platform can be chosen to improve multiple performance criteria, such as increasing the likelihood of detection of an object, or adjusting how closely measurements should be spaced.

I. INTRODUCTION

In this work, three point pattern estimators from the field of point pattern analysis (PPA) are used to study scans from a pitching multi-beam Lidar (MBL). MBLs typically have high resolution in the horizontal plane, but relatively worse resolution along the vertical axis. This problem can be overcome by placing the Lidar on a pitching platform, which adds an extra degree of freedom to the sensor. The choice of the pitching trajectory and the trajectory parameters can improve the vertical resolution. However, the resulting scan distributions, while repeatable, are not uniformly distributed within the field of view. The distributions of measurements from the rotating MBL (RMBL) are treated as point patterns to quantify the scan performance. Three functions from the field of PPA [1], [2], [3] are introduced and applied to simulated RMBL scans employing different scanning trajectories to understand what phenomenon each function quantifies. A design example is presented that demonstrates how these estimators can be used to select a desirable scanning trajectory to improve the scan's resolution.

Lidar sensors measure distance by emitting pulsed laser light, detecting the reflected particles, and then converting the time of flight of the particles into a distance. Lidar has a long history [4] but has recently gained popularity in robotics, especially unmanned and autonomous vehicles [5], [6], [7], which has led to an increase in the availability and performance of the sensors. Of particular note is their recent use in self-driving cars, where MBL sensors are used to segment and classify the road surface, curbs, other cars, pedestrians, and various other objects [8], [9], [10], [11]. Current Lidar technology allows for sensors that can capture 3-dimensional distance data inherently by rotating

This work was supported in part by the NSF through OISE-1658696.

¹Michael Benson, Jonathan Nikolaidis, and Garrett Clayton are with the Department of Mechanical Engineering, Villanova University, Villanova, PA 19085, USA garrett.clayton@villanova.edu

an array of emitters/detectors which are mounted at distinct angles from the horizontal plane. Each emitter/detector can be sampled at very high frequencies (10s of kHz), but there are limitations on how closely the sensing elements can be placed. As a result, MBLs commonly have high resolution in the horizontal plane (limited by sampling rate), but relatively worse resolution along the vertical axis (limited by sensor element placement). This limitation can result in poor detection or classification performance of the system. Placing an MBL on a rotating platform can improve the vertical resolution [12], [13], but the trajectory for the added degree of freedom must be chosen carefully to provide a desirable sampling of the environment.

While MBL typically have fixed, evenly-spaced sampling patterns, pitching the MBL causes the measurements to be irregularly distributed, and thus RMBL scans can be complex to analyze, limiting a deeper understanding of sampling behaviors, such as resolution. Similar scan patterns were studied when rotating single-beam Lidar (RSBL) configurations were common [14], [15], but that analysis has not been extended to RMBL sensors. Methods to quantify RSBL resolution, such as counting the number of times the beam paths intersect [15], are typically trajectory dependant and don't scale well to RMBL. Methods from other fields, such as the use of Voronoi tessellation to measure spatial resolution in high-speed scanning probe microscopy [16], can be used, but are very computationally expensive for RMBL scans which have tens of thousands to hundreds of thousands of samples. One work of note is from Morales et al., which used Ripley's K function, a metric from the field of PPA, to analyze the homogeneity of RMBL scans [12]. In that work, Ripley's K function was used a goodness-of-fit test to determine whether their RMBL scans could be modeled as a homogeneous Poisson point process (HPPP), which has desirable key properties for scanning.

Point pattern analysis traditionally uses a collection of functions as goodness-of-fit tests, as in [12], to determine whether a point pattern is a result of some underlying process (e.g., Poisson). However, in this work some of these functions are instead employed and modified to quantify and analyze how measurements in the scan are distributed. These functions are used to provide both numerical evaluation and physical understanding of RMBL scans taken by any arbitrary trajectory. Note that, while this work focuses on RMBL systems, these estimators may have relevance in applications such as scanning fiber endoscopes, scanning probe microscopy, or other applications involving an actuated sensing mechanism with a single or multiple point sensor.

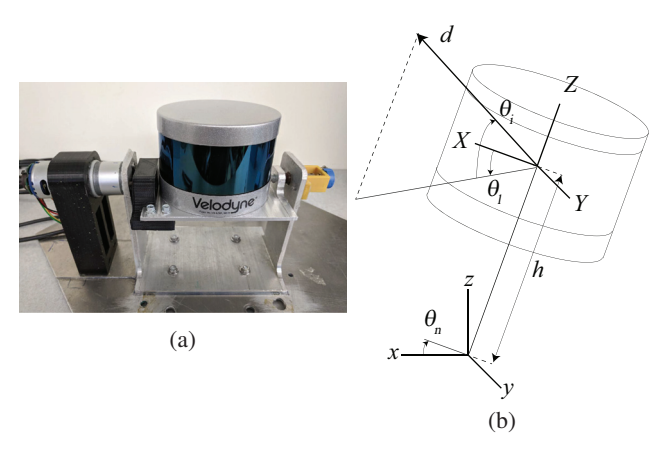


Fig. 1: a) The experimental pitching multi-beam Lidar platform. b) Relevant geometry of the platform.

II. PROBLEM FORMULATION

In this section, the RMBL system used by the authors is presented, two pitching trajectories for the RMBL are shown, and notation used in the remainder of the paper is provided.

A. Rotating MBL Platform

The experimental pitching RMBL used in this work is shown in Figure 1a. A Velodyne VLP-16 Lidar is situated on a cradle capable of $\pm 90^{\circ}$ pitching motion. While the VLP-16 is not the highest resolution Lidar available, it is certainly one of the most affordable commercially available MBLs (and the work in this paper can easily be applied to other MBL sensors). The VLP-16 features 16 beams evenly spaced over a $\pm 15^{\circ}$ vertical field of view (FOV), providing 2° vertical resolution. The array of beams is spun at 20Hz, and each beam is sampled 900 times per revolution, resulting in 0.4° horizontal resolution. The cradle is driven by a DC motor, and potentiometer and encoder data are fused to provide the cradle angle. Control of the motor is performed using an Arduino Due, and a Jetson TK1 controls trajectory parameters, aggregates point clouds, and provides real time data visualization. The software on both the Arduino Due and the Jetson TK1 are developed using the Robotics Operating System (ROS) middleware.

The geometry of the RMBL configuration is shown in Figure 1b. The array of beams in the Lidar spin with angle θ_l about the Z body-fixed axis. Each beam has a unique inclination angle θ_i above the XY-plane and returns a distance measurement d (if there is an object within the range of the Lidar). The DC motor pitches the cradle with angle θ_n about the y-axis. An offset height h exists between the cradle's axis of rotation and the Lidar's sensor origin XYZ, so θ_n imparts both rotation and translation of the XYZ-frame.

Points from the Lidar are received with spherical coordinates (d, θ_i, θ_l) in the XYZ-frame and are transformed into Cartesian coordinates in the fixed xyz-frame:

$$d_x = d\cos\theta_i\cos\theta_l\cos\theta_n - d\sin\theta_i\sin\theta_n - h\sin\theta_n, \quad (1)$$

$$d_{ii} = d\cos\theta_i \sin\theta_l,\tag{2}$$

$$d_z = d\cos\theta_i\cos\theta_l\sin\theta_n + d\sin\theta_i\cos\theta_n + h\cos\theta_n.$$
 (3)

When the beams are facing towards the front or back of the FOV $\theta_l \approx 0, \approx \pm \pi$, changes in the pitching angle θ_n result in large changes in the orientation of the beams. However, when the beams are facing towards the side of the FOV $\theta \approx \pm \pi/2$, changes in the pitching angle result in small changes in the orientation of the beam. As a result, scans from the RMBL tend to be more clustered along the y-axis, and more dispersed along the x-axis.

For modeling and analysis in this work, RMBL scans are simulated for scanning the surface \mathbb{S}^2 of a hollow unit sphere centered at the xyz origin. Investigation of the scan on the unit sphere allows for analysis of the distribution as a result of the chosen trajectory without dependency on the Lidar's environment. Measurement points are converted from Cartesian coordinates in the xyz-frame into spherical coordinates in the xyz-frame with latitude ϕ , azimuth (or longitude) θ , and radius r:

$$\phi = \operatorname{atan2}(d_z, \sqrt{d_x^2 + d_y^2}),\tag{4}$$

$$\theta = \operatorname{atan2}(d_y, d_x),\tag{5}$$

$$r = 1. (6)$$

Because the radius measurement r=1 is the same for all measurements, it can be ignored for the analysis, allowing the problem to be collapsed from 3- to 2-dimensions. The analysis of how the scan would interpret an object of a given size and distance is performed by projecting the object onto the unit sphere.

B. RMBL Trajectories

Perhaps the most common scan pattern for a pitching Lidar is the raster scan pattern. Traditionally a raster scan pattern involves the collection of measurements along a number of parallel line paths. Each of the lines is dubbed a "raster line" n_r , and the scan period T_n increases proportionally with increasing n_r .

The MBL used in this work continuously performs a 360° rotation of the beams at $f_l = 20Hz$:

$$\theta_l(t) = \pi - (2\pi f_l t \bmod 2\pi). \tag{7}$$

Due to this constant spinning motion, a raster-like trajectory can be accomplished by pitching the Lidar after each complete rotation of the beams. The rotating platform is moved in a stair-step pattern with trajectory:

$$\theta_n(t) = -A + 2A \frac{\lfloor f_l t \rfloor}{\frac{n_r}{n_b} - 1}, \quad \frac{n_r}{n_b} \in \mathbb{Z} > 1,$$
 (8)

where n_b is the number of beams in the MBL, 2A is the peak-to-peak amplitude of the scan, $\lfloor x \rfloor$ is the floor of x, and the total period of the scan in seconds is $T_n = \frac{n_r}{n_b} \frac{1}{f_t}$.

Hence, the cradle is moved in equal intervals to perform a raster-style scan (henceforth, referred to as a "raster scan").

Another trajectory used in this work is a Lissajous-like trajectory. A classical Lissajous scan involves rotating both axes of a dual-axis sensor with sinusoidal trajectories. In this work, the rotation of the lasers $\dot{\theta}_l$ is fixed (as stated before), and the pitching cradle undergoes a triangular trajectory:

$$\theta_n(t) = \frac{2A}{T_n} \left(t - \frac{T_n}{2} \left\lfloor \frac{2t}{T_n} + \frac{1}{2} \right\rfloor \right) (-1)^{\lfloor \frac{2t}{T_n} + \frac{1}{2} \rfloor}. \tag{9}$$

The triangular trajectory is chosen as it provides a more uniform distribution of points along the vertical axis, as opposed to a sinusoidal trajectory which biases points towards the top and bottom of the trajectory. This trajectory is "Lissajous-like" because, while it is not a traditional Lissajous trajectory, the behavior and analysis are similar.

The raster and Lissajous-like trajectories each have their own relative strengths and weaknesses [13]. However, the relative merits are not relevant to the scope of this work, and thus are not discussed here.

C. Notation

In order to present the metrics used, the relevant notation is presented in this section, which is borrowed from spatial statistics [3]. Define \mathbf{X} as a finite point process with a set of measurement locations $\underline{\mathbf{x}} = \{x_1, ..., x_n\}$ from the RMBL on the unit sphere \mathbb{S}^2 such that $x_j \in \mathbb{S}^2$, with each point x_j consisting of a latitude ϕ_j and longitude angle θ_j . Note that this point pattern possibly contains redundant measurements.

The intersection of a plane in \mathbb{R}^3 and the sphere \mathbb{S}^2 is called a *great circle* if the plane passes through the sphere's origin. The geodesic distance d(u,v) between two points u and v on \mathbb{S}^2 is the shortest path along the great circle which passes through both points. The geodesic distance from any point $u \in \mathbb{S}^2$ to a set $B \in \mathbb{S}^2$ is defined as $d(u,B) = \inf\{d(u,v) : v \in B\}$.

The indicator function $\mathbb{1}(y)$ is used in this work, which is a function that returns 1 if the condition y is true, and 0 otherwise.

III. POINT PATTERN ESTIMATORS

Summary functions, or functions applying to the entire region of the unit sphere, can be used to estimate the properties of the underlying point process from the RMBL X. Specifically, three estimators are used in this work:

- Ripley's K function, which estimates the number of measurements in an area (or the density of measurements),
- the nearest neighbor function G, which estimates the distance to a measurement's nearest neighboring measurement in the scan,
- the empty-space function F, which estimates the distance to the nearest measurement for a random location on the surface \mathbb{S}^2 .

All three estimators are functions of r, which in the context of the unit sphere is a geodesic distance (as opposed to typically using r as a radius for planar analysis).

To demonstrate the three estimators, three simulated scans, which are shown in Figure 2, are presented:

- A single, stationary scan of the MBL $A=0^{\circ}, T_n=0.05s$.
- A pitching raster scan, $A = 75^{\circ}$, $T_n = 0.3s$,
- A pitching Lissajous-like scan, $A = 15^{\circ}$, $T_n = 0.15s$.

The stationary scan demonstrates the high horizontal resolution but the relatively worse vertical resolution of the MBL sensor (with no pitching motion). The raster scan is chosen to provide a scan with full coverage of the unit sphere but with approximately the same resolution as that of the stationary scan (the "step" sizes for the raster scan are 30°, the same as the vertical FOV of the sensor). The Lissajous-like scan is chosen to demonstrate a scan with a smaller FOV (than the raster), but with improved vertical resolution.

A. Ripley's K Function

Ripley's K function K(r) calculates the average number of points in the set $\underline{\mathbf{x}}$ that fall within the range r of a typical point of $\underline{\mathbf{x}}$:

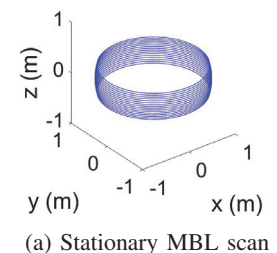
$$\hat{K}(r) = \frac{1}{n(\underline{\mathbf{x}})} \sum_{x \in \underline{\mathbf{x}}} \sum_{\substack{x' \in \underline{\mathbf{x}} \\ x' \neq x}} \mathbb{1} \{ d(x, x') \le r \}, \tag{10}$$

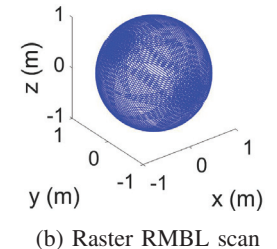
where $n(\underline{\mathbf{x}})$ is the number of points in the set $\underline{\mathbf{x}}$ and $0 \le r \le \pi$. When operating on the unit sphere, $\hat{K}(r)$ is the average number of points that fall in a spherical cap with geodesic distance r from its apex at a point in $\underline{\mathbf{x}}$ to the edge of the cap. This can, for example, be used to estimate how many measurements the RMBL will yield for an object by projecting that object onto the unit sphere and finding an appropriate size r that encompasses that object's projection. Scans with larger values of $\hat{K}(r)$ will return more measurements of an object with cap size r (compared to smaller values of $\hat{K}(r)$).

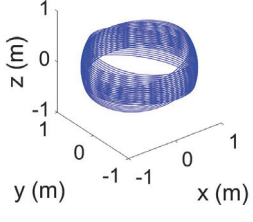
Figure 3 displays the values of $\hat{K}(r)$ for the three scans shown in Figure 2, and also provides bars for ± 1 standard deviation in the number of measurements for each evaluated radius r. The raster scan, which has the largest total number of samples, has larger values of $\hat{K}(r)$, and thus would return more measurements of an object on average than the Lissajous-like or stationary scans. All three scans have relatively large standard deviations, as the scans are not uniformly distributed, and thus the number of measurements vary greatly until the entire sphere is measured at $r=180^\circ$. Of note is that the values of the standard deviation decrease near $r\approx 90^\circ$. This is because the RMBL scans tend to be nearly symmetric about some vertical plane, so caps spanning half of the sphere have approximately the same number of measurements as a cap drawn opposite it on the sphere.

B. Nearest Neighbor Function

The nearest neighbor function $\hat{G}(r)$ calculates the percentage of points in the set $\underline{\mathbf{x}}$ whose distance to their nearest neighboring measurements are less than or equal to r:







(c) Lissajous-like RMBL scan

Fig. 2: Point clouds of simulated scans of a unit sphere by a) a stationary scan from the VLP-16 MBL, b) an RMBL raster scan with $A = 75^{\circ}$, $T_n = 0.3s$, and c) an RMBL Lissajous-like scan with $A = 15^{\circ}$, $T_n = 0.15s$.

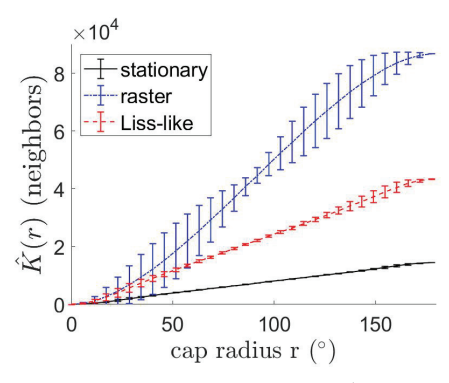


Fig. 3: Values of Ripley's K function $\hat{K}(r)$ for three simulated RMBL scans, with ± 1 standard deviation in the number of neighboring measurements for each evaluated radius r.

$$\hat{G}(r) = \frac{1}{n(\underline{\mathbf{x}})} \sum_{x \in \underline{\mathbf{x}}} \mathbb{1} \{ d(x, \underline{\mathbf{x}} \backslash x) \le r \}, \tag{11}$$

with $0 \le r \le \pi$. In other words, $\hat{G}(r)$ is the cumulative distribution function of nearest neighbor distances. This can loosely be used as a way to look at the "resolution" of the scan by analyzing how close measurements are to one another. Larger values of $\hat{G}(r)$ for a given value of r indicates that more samples have nearest neighbors within that distance, and hence are closer to each other (than for a smaller value of $\hat{G}(r)$).

Figure 4a shows the values of $\hat{G}(r)$ for the three scans presented in the previous section. The stationary scan $\hat{G}(r)$ is a step function with the step at $r=360/900=0.4^\circ$ which is the MBL's horizontal resolution. The raster and Lissajous-like scans have some measurements that are closer together, which mostly occur toward the sides of the scan where they are clustered together. However, more than half the measurements still have nearest neighbors about 0.4° away. To provide a better understanding of how the pitching motion has improved the vertical resolution, a "ring-blind" variant of the nearest neighbor function is introduced. In this variant of the nearest neighbors from the same beam of the Lidar from the same 360° rotation of the beams (e.g., measurements from the same "ring" as one would see in the stationary scan) are ignored.

Figure 4b presents $\hat{G}_{ring}(r)$ for the three scans presented earlier. The stationary scan now yields a step function at $r=2^{\circ}$ which is the vertical resolution of the MBL. There is now more information about the distribution of measurements for the raster and Lissajous-like scans. The Lissajous-like scan has closer neighbors than the raster scan for the majority of its points. This is due to the Lissajous-like scan having better coverage of its FOV, while the raster scan effectively takes multiple stationary scans with different FOVs that only overlap at the sides of the scan. However, both pitching scans still have relatively large steps at $r=2^{\circ}$ due to areas at the edge of the scan's FOV where there are no overlapping beam paths, resulting in nearest neighbors from the beams directly above or below a given measurement.

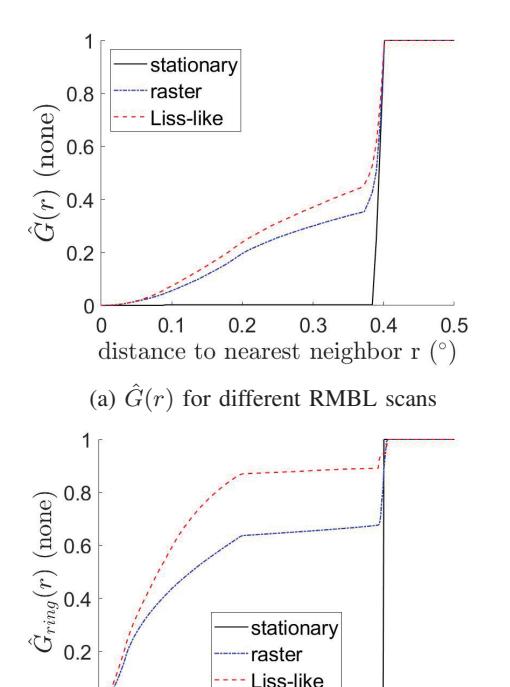
C. Empty Space Function

The empty space function $\hat{F}(r)$ calculates the amount of "empty space", or the amount of the unit sphere that isn't covered by the set of measurements. In this work, $\hat{F}(r)$ is calculated by simulating m evaluation points $\underline{\mathbf{y}}$ uniformly distributed over the unit sphere and then calculating the percentage of evaluation points whose minimum distance to the set is less than r:

$$\hat{F}(r) = \frac{1}{m} \sum_{y \in \mathbf{y}} \mathbb{1}(d(y, \underline{\mathbf{x}}) \le r), \tag{12}$$

with $0 \le r \le \pi$. In other words, this function is the cumulative distribution function of how many evaluation points have nearest neighboring measurements within a geodesic distance r, and represents the empty space in the scan provided $\underline{\mathbf{y}}$ adequately samples the unit sphere. A function $\hat{F}(r)$ that rises quickly to 1 indicates that random sample points have small distances r to measurements in the scan, and hence there is less "empty space" in the scan (compared to smaller values of $\hat{F}(r)$). $\hat{F}(r)$ provides a method to estimate the likelihood of a particular scan's ability to detect objects in a region of interest. The larger the values of $\hat{F}(r)$, the higher the probability of detection, as the higher the likelihood the object is closer to (at least one sample in) the scan.

Figure 5 shows the empty space function $\hat{F}(r)$ for the three scans presented earlier. The raster scan has much greater values of $\hat{F}(r)$, and thus far less empty space, because it spans the entire sphere, while the Lissajous-like and



distance to nearest neighbor r (°) (b) $\hat{G}_{ring}(r)$ for different RMBL scans

1.5

2

2.5

Fig. 4: a) The nearest neighbor function $\hat{G}(r)$ for the stationary, raster, and Lissajous-like (Liss-like) scans. b) The ring-blind variant of the nearest neighbor function $\hat{G}_{ring}(r)$ for the same scans.

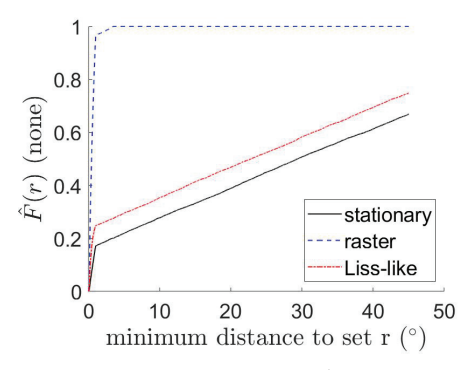


Fig. 5: The empty space function $\hat{F}(r)$ for the stationary, raster, and Lissajous-like scans.

stationary scans have significantly more empty space because they do not cover large sections of the top and bottom of the sphere. The Lissajous-like scan is also observed to have less empty space than the stationary scan. This is because it has a slightly larger FOV (causing the constant offset for $r>1^\circ$), and because it has more points closer together within its FOV (causing the larger jump at $r\leq 1^\circ$).

D. Local Point Pattern Estimation

While the results shown in this section so far have been for PPA estimators applied over the entire unit sphere, each

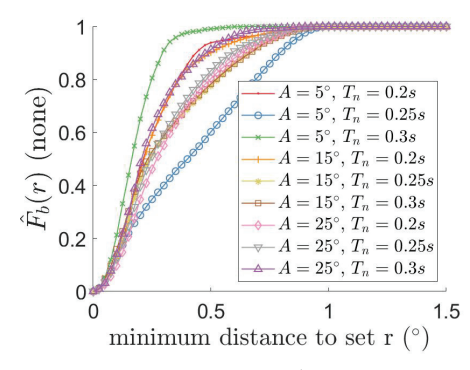


Fig. 6: Empty space function $\hat{F}(r)$ in the cross-section $-15^{\circ} \leq \theta \leq 15^{\circ}, -15^{\circ} \leq \phi \leq 15^{\circ}$ for a series of Lissajous-like scans.

function can also be evaluated for subsets of the set $\underline{\mathbf{x}}$ occurring in a region of the unit sphere W. When evaluating these local estimators on a region W, they are prone to edge effect distortions [3], which were not present in the summary estimates because the full unit sphere has no edges. These edge effect biases occur because points near the edge of the region will have fewer valid neighbors (some neighbors will not be in W). In this work, a simple and commonly-used method of edge correction called the border method is used [3]. Border-corrected, local calculations of the estimators in this paper are denoted with the subscript $_b$, e.g., $\hat{K}_b(r)$.

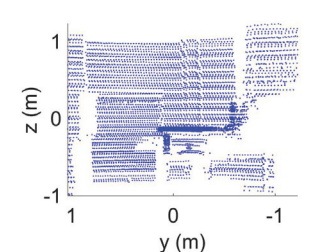
IV. DESIGN EXAMPLE: IMPROVING DETECTION PERFORMANCE

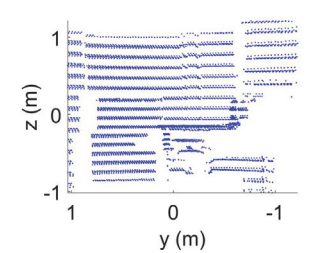
The estimators presented in Section III can be used to help select a scan with desirable performance. As an example, this section seeks to identify a high-frequency scan that has the best chance of detecting an object of random size and distance in the region of interest in front of the RMBL $-15^{\circ} \leq \theta \leq 15^{\circ}, -15^{\circ} \leq \phi \leq 15^{\circ}$. Lissajous-like scans with amplitudes $A = \{5^{\circ}, 15^{\circ}, 25^{\circ}\}$ and periods of $T_n = \{0.2s, 0.25s, 0.3s\}$ are simulated, and then the bordercorrected empty space function for the region of interest is calculated. The results for F(r) are shown in Figure 6. Interestingly, there do not appear to be distinct relationships between the value of $\hat{F}(r)$ and the scan amplitude or period. For example, the 5°, 4Hz scan has smaller values of $\hat{F}(r)$ than the 5° , 5Hz scan, despite having a larger period, which is contrary to an initial expectation of scans with larger periods having less empty space.

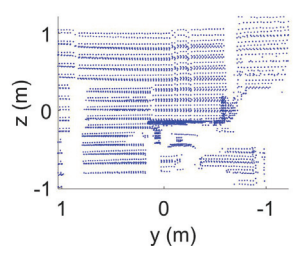
The scan with the largest area under the curve for $\hat{F}(r)$ should have the best detection performance, as it has the least empty space in the region of interest. Accordingly, the 5° , 3.33Hz scan is selected as the "best" performing scan, and the 5° , 4Hz scan is selected as the "worst" performing scan. To demonstrate this, experimental RMBL scans of the space shown in Figure 7a are presented in Figures 7b-d using the same region of interest as in the prior paragraph. The "best" scan, shown in Figure 7b, is well distributed across the space, and should observe any sufficiently sized object that doesn't fall between the very close point spacings. However, in the



(a) Color image of space to be sampled







(b) Lissajous-like Scan with $T_n=$ (c) Lissajous-like Scan with $T_n=$ (d) Lissajous-like Scan with $T_n=0.3s$ 0.25s 0.25

Fig. 7: Cross-sections of the front of point clouds from experimental Lissajous-like scans with $A=5^{\circ}$ and periods of a) 3.33Hz, b) 4Hz, and c) 5Hz.

"worst" scan, shown in Figure 7c, the pitching trajectory causes multiple rotations of the beams to almost overlap, leaving large un-scanned spaces between the paths of the beams. The 5° , 5Hz scan is also shown in Figure 7d to demonstrate the aforementioned observation that there is not a distinct trend with respect to $\hat{F}(r)$ as a function of the period: the 5Hz scan has less empty space than the 4Hz scan despite having fewer total samples.

V. CONCLUSIONS

In this paper, a pitching multi-beam Lidar was presented to overcome the vertical resolution limitation in stationary multi-beam Lidar, and two pitching trajectories were discussed. Three estimators from the field of point pattern analysis were presented to study the distribution of measurements from this pitching multi-beam Lidar. These three estimators were applied to various simulated scans, both over the entirety of the unit sphere as well as bounded sub-sections of the sphere, and the findings were linked to observations in experimental scans with the same trajectory parameters.

Each of the three presented estimators has particular relevance to robotics and unmanned vehicle applications. The Ripley's K function allows for estimation of how many measurements will be returned by a scan for an object of known shape, size, and distance, which has possible usefulness in classification tasks. The nearest neighbor function can be used to estimate how close a neighboring measurement should be, which could aid in segmentation tasks. Finally, the empty space function determines the amount of un-sampled space in the field of view, which has obvious relevance to detection tasks.

While the presented estimators have potential use in both Lidar and other fields, it is very important to note that each metric describes very particular and specific behavior. For example, if using the nearest-neighbor function alone, it is possible that a scan which causes $\hat{G}(r)$ to quickly climb to $\hat{G}(r)=1$ may not desirably sample the space. In the worst case, a scan that causes that behavior in the nearest-neighbor function would have every point at approximately the same location. While this provides favorable values of $\hat{G}(r)$, it does not provide an adequate sampling of the space

in most cases. Thus, it is important to employ multiple metrics collaboratively.

REFERENCES

- [1] B. D. Ripley, "Modelling spatial patterns," *Journal of the Royal Statistical Society: Series B (Methodological)*, vol. 39, no. 2, pp. 172–192, 1977.
- [2] —, Spatial statistics. John Wiley & Sons, 2005, vol. 575.
- [3] T. Lawrence, A. Baddeley, R. K. Milne, and G. Nair, "Point pattern analysis on a region of a sphere," *Stat*, vol. 5, no. 1, pp. 144–157, 2016.
- [4] T. Neff, *The Laser That's Changing the World.* Prometheus Books, 2018
- [5] S. Kohlbrecher, O. Von Stryk, J. Meyer, and U. Klingauf, "A flexible and scalable slam system with full 3d motion estimation," in 2011 IEEE International Symposium on Safety, Security, and Rescue Robotics. IEEE, 2011, pp. 155–160.
- [6] J. Fuentes-Pacheco, J. Ruiz-Ascencio, and J. M. Rendón-Mancha, "Visual simultaneous localization and mapping: a survey," *Artificial Intelligence Review*, vol. 43, no. 1, pp. 55–81, 2015.
- [7] W. Hess, D. Kohler, H. Rapp, and D. Andor, "Real-time loop closure in 2d lidar slam," in 2016 IEEE International Conference on Robotics and Automation (ICRA). IEEE, 2016, pp. 1271–1278.
- [8] M. S. Darms, P. E. Rybski, C. Baker, and C. Urmson, "Obstacle detection and tracking for the urban challenge," *IEEE Transactions on intelligent transportation systems*, vol. 10, no. 3, pp. 475–485, 2009.
- [9] W. Zhang, "Lidar-based road and road-edge detection," in 2010 IEEE Intelligent Vehicles Symposium. IEEE, 2010, pp. 845–848.
- [10] J. Han, D. Kim, M. Lee, and M. Sunwoo, "Enhanced road boundary and obstacle detection using a downward-looking lidar sensor," *IEEE Transactions on Vehicular Technology*, vol. 61, no. 3, pp. 971–985, 2012.
- [11] H. Gao, B. Cheng, J. Wang, K. Li, J. Zhao, and D. Li, "Object classification using cnn-based fusion of vision and lidar in autonomous vehicle environment," *IEEE Transactions on Industrial Informatics*, vol. 14, no. 9, pp. 4224–4231, 2018.
- [12] J. Morales, V. Plaza-Leiva, A. Mandow, J. A. Gomez-Ruiz, J. Serón, and A. García-Cerezo, "Analysis of 3d scan measurement distribution with application to a multi-beam lidar on a rotating platform," *Sensors*, vol. 18, no. 2, p. 395, 2018.
- [13] M. Benson, J. Nikolaidis, and G. M. Clayton, "Lissajous-like scan pattern for a nodding multi-beam lidar," in ASME 2018 Dynamic Systems and Control Conference. American Society of Mechanical Engineers, 2018, pp. V002T24A007–V002T24A007.
- [14] A. Bazaei, Y. Yong, and S. Moheimani, "High-speed Lissajous-scan atomic force microscopy: Scan pattern planning and control design issues," *Review of Scientific Instruments*, vol. 83, no. 6, p. 063701, 2012.
- [15] J. W. Anderson and G. M. Clayton, "Lissajous-like scan pattern for a gimballed lidar," in Advanced Intelligent Mechatronics (AIM), 2014 IEEE/ASME International Conference on. IEEE, 2014, pp. 1171–1176. [Online]. Available: http://ieeexplore.ieee.org/abstract/document/6878240/
- [16] T. Tuma, J. Lygeros, A. Sebastian, and A. Pantazi, "Optimal scan trajectories for high-speed scanning probe microscopy," in 2012 American Control Conference (ACC). IEEE, 2012, pp. 3791–3796.